APL Photonics

RESEARCH ARTICLE | MAY 02 2025

Electrically tunable liquid-crystal metasurfaces with patterned birefringence and dichroism

Special Collection: Angular Momentum of Light

Paola Savarese ; Sarvesh Bansal ; Maria Gorizia Ammendola ; Raouf Barboza ; Marcella Salvatore ; Stefano Luigi Oscurato ; Bruno Piccirillo ; Francesco Di Colandrea ; Lorenzo Marrucci ; Filippo Cardano

APL Photonics 10, 050802 (2025)
https://doi.org/10.1063/5.0261491

Electrically tunable liquid-crystal metasurfaces with patterned birefringence and dichroism

Cite as: APL Photon. 10, 050802 (2025); doi: 10.1063/5.0261491
Submitted: 30 January 2025 • Accepted: 15 April 2025 •
Published Online: 2 May 2025

Paola Savarese,[1] Sarvesh Bansal,[1] Maria Gorizia Ammendola,[1,2] Raouf Barboza,[3] Marcella Salvatore,[1] Stefano Luigi Oscurato,[1] Bruno Piccirillo,[1] Francesco Di Colandrea,[1,a)] Lorenzo Marrucci,[1,4] and Filippo Cardano[1,a)]

AFFILIATIONS

[1] Dipartimento di Fisica "Ettore Pancini", Università degli Studi di Napoli Federico II, Complesso Universitario di Monte Sant'Angelo, Via Cintia, 80126 Napoli, Italy
[2] Scuola Superiore Meridionale, Via Mezzocannone, 4, 80138 Napoli, Italy
[3] Dipartimento di Scienze e Ingegneria della Materia, dell'Ambiente ed Urbanistica, Università Politecnica delle Marche, Via Brecce Bianche, 60131 Ancona, Italy
[4] CNR-ISASI, Institute of Applied Science and Intelligent Systems, Via Campi Flegrei 34, 80078 Pozzuoli (NA), Italy

Note: This paper is part of the Special Topic on Angular Momentum of Light.
[a)] **Authors to whom correspondence should be addressed:** francesco.dicolandrea@unina.it and filippo.cardano2@unina.it

ABSTRACT

Light propagation through artificially patterned anisotropic materials, such as dielectric metasurfaces, enables precise control of the spatio-vectorial properties of optical fields using highly transparent, thin, and flat optical elements. Liquid-crystal cells are a common realization of such devices. Optical losses are typically assumed to be polarization-independent and are therefore often overlooked in modeling these systems. In this work, we introduce electrically tunable liquid-crystal metasurfaces with patterned birefringence and dichroism, achieved by incorporating dichroic dye molecules into the liquid-crystal mixture. These dye molecules align with the liquid crystal, effectively coupling birefringence and dichroism effects. The behavior of these metasurfaces is described using non-unitary Jones matrices, validated through polarimetric measurements. In the case of devices that are patterned to form polarization gratings, we also characterize the diffraction efficiency as a function of the dichroism and birefringence parameters, which can be tuned jointly by applying an electric field across the cell. This study not only introduces a new class of optical components but also deepens our understanding of light propagation through anisotropic materials, where dichroism can naturally arise from bulk material properties or from reflection and transmission laws at their interfaces.

I. INTRODUCTION

Spin–orbit photonic technologies allow for accurate manipulation of spatio-vectorial features of optical fields by acting on optical polarization in a space-dependent manner.[1,2] Their capability of generating structured light enables relevant applications, including particle trapping,[3,4] robust light guidance,[5,6] imaging,[7–9] and simulation of spin-dependent dynamics.[10] Spin–orbit interactions of light also play a crucial role in topological photonics,[11] underlying the observation of unique phenomena, such as the subwavelength displacement of a circularly polarized beam at an interface, which is a typical manifestation of the spin-Hall effect of light.[12–14]

In the past decades, this functionality has been demonstrated for a variety of anisotropic materials, such as photonic crystals,[15,16] liquid crystals,[17–19] epsilon-near-zero materials,[20] as well as plasmonic[21–23] and dielectric metasurfaces.[24–26] In this context, liquid-crystal metasurfaces (LCMSs), slabs of nematic liquid crystals (LCs) artificially patterned on the micrometric scale,[27] emerge as a versatile and compact solution to structure light polarization and beam transverse profile.[28,29] Although they lack the characteristic subwavelength patterning of typical nanostructures, these devices

achieve metasurface-like functionalities by exploiting gradients of the Pancharatnam–Berry phase to tailor optical beams across a wide spectral range.[30] In this case, the functional subunits are not discrete meta-atoms but local domains in the continuous LC medium, defined by the molecular director orientation. The prototypical example of LCMSs is the q-plate,[31] wherein the liquid-crystal layer is aligned with an integer or semi-integer topological charge, which allows for partial or full conversion of spin angular momentum into orbital angular momentum. Since their first introduction, LCMSs have found applications in both classical and quantum domains,[32] in particular microscopy,[33] communications,[34,35] metrology,[36,37] and simulations.[10,38,39]

In all experiments involving q-plates and their generalization to arbitrarily patterned devices, optical losses across the LC slab have been assumed to be polarization-independent; therefore, no measurable effect was revealed, apart from a global attenuation of the incoming light intensity. Exceptions can be found in the context of LC polarization gratings, introduced specifically for polarization holography and polarization imaging.[40–42] In this paper, we go beyond this regime and extend the functionality of LCMSs to the case of polarization-dependent optical losses. In particular, these are introduced by doping the LC mixture with dichroic dye molecules, featuring differential absorption for two orthogonal polarization components. We show that the response of this new class of LCMSs can be effectively modeled as a non-unitary Jones matrix, where the distance from the unitary case is proportional to the dichroic power of the cell. This formalism has also been adopted in previous studies, reporting, for instance, POLICRYPS-based diffraction gratings, where the dichroic character stems from the polarization-dependent diffraction efficiency of the sample, measured by rotating the analyzer direction.[43] Similarly, a recent study introduced thermally tunable dichroic LMCSs acting as circular polarization gratings.[44] In this work, we present dichroic LCMSs that are instead electrically tunable, that is, when an electric field is applied across the cell, a torque on the LC molecules tilts them out of the slab plane, modifying both birefringence and dichroism. This model is experimentally validated on a few samples of dichroic LCMSs, in the case of both uniform and spatially patterned optic-axis orientations. In the latter scenario, we specifically focus on polarization gratings, given their use in several fields, and provide a characterization of their diffraction efficiency as a function of the dichroic parameter, based on the recorded far-field patterns.

II. DICHROIC LCMSs

LCMSs can be effectively modeled as slabs of birefringent uniaxial materials.[45] Their action is typically described through the Jones formalism, where the field is described by a 2D complex vector. The vector entries represent the complex amplitudes of the field associated with two orthogonal polarization states, serving as a basis. If diffraction within the sample can be neglected, the output field of the LCMS is obtained by applying the device's Jones matrix to the input Jones vector. To begin, we consider a LCMS with a uniform pattern. In the basis of the extraordinary and ordinary axes, the Jones matrix for such a system is expressed as

$$\mathcal{L} = \begin{pmatrix} e^{ikn_e d} & 0 \\ 0 & e^{ikn_o d} \end{pmatrix}, \tag{1}$$

where $k = 2\pi/\lambda$ is the incident light wave vector, with λ being the optical wavelength; n_e (n_o) is the refractive index along the extraordinary (ordinary) axis; and d is the sample thickness. For simplicity, we can assume that the extraordinary (ordinary) axis coincides with the x (y) direction, and photons propagate along z. This model is compatible with polarization-independent losses, which affect the propagation of two polarization components in the same way and can therefore be neglected.

We aim to introduce linear dichroism in our device, which corresponds to differential absorption depending on the input linear polarization. In LC displays, a typical solution relies on the so-called *guest–host* effect,[46] wherein a guest dichroic compound, such as an absorbing dye, is incorporated into the host LC matrix. In our experiment, the LC mixture is doped with organic dye molecules, specifically 1,4-diaminoanthraquinone. The Jones matrix in Eq. (1) is thus generalized as

$$\mathcal{L} = \begin{pmatrix} e^{ikn_e d} e^{-\alpha_e d} & 0 \\ 0 & e^{ikn_o d} e^{-\alpha_o d} \end{pmatrix}, \tag{2}$$

where α_e (α_o) is the absorption coefficient along the extraordinary (ordinary) axis, typically with $\alpha_e > \alpha_o$.[47] The matrix in Eq. (2) is indeed a non-unitary Jones matrix, whose birefringence and dichroism can be formally combined as follows:

$$\mathcal{L} = e^{i\tilde{\zeta}/2} \begin{pmatrix} e^{i\zeta/2} & 0 \\ 0 & e^{-i\zeta/2} \end{pmatrix}, \tag{3}$$

where $\zeta = \delta + i\eta$ and $\tilde{\zeta} = \tilde{\delta} + i\tilde{\eta}$ are complex parameters, with

$$\begin{aligned} \delta &= kd(n_e - n_o), \\ \eta &= d(\alpha_e - \alpha_0), \\ \tilde{\delta} &= kd(n_e + n_o), \\ \tilde{\eta} &= d(\alpha_e + \alpha_o). \end{aligned} \tag{4}$$

In Eq. (3), $e^{i\tilde{\zeta}/2}$ accounts for a global phase shift and attenuation factor.

If the LC molecules lie at an angle θ in the xy plane, the dye molecules align with the underlying birefringent host.[46] Accordingly, the Jones matrix in Eq. (3) is transformed as

$$\mathcal{L}_\theta = e^{i\tilde{\zeta}/2} \begin{pmatrix} \cos\frac{\zeta}{2} + i\sin\frac{\zeta}{2}\cos 2\theta & i\sin\frac{\zeta}{2}\sin 2\theta \\ i\sin\frac{\zeta}{2}\sin 2\theta & \cos\frac{\zeta}{2} - i\sin\frac{\zeta}{2}\cos 2\theta \end{pmatrix}. \tag{5}$$

The latter assumes a simpler expression in the circular polarization basis, where $|L\rangle = (1,0)^T$ ($|R\rangle = (0,1)^T$) is the left-handed (right-handed) circular polarization state:

$$\mathcal{L}_\theta = e^{i\tilde{\zeta}/2} \begin{pmatrix} \cos\frac{\zeta}{2} & i\sin\frac{\zeta}{2}e^{-2i\theta} \\ i\sin\frac{\zeta}{2}e^{2i\theta} & \cos\frac{\zeta}{2} \end{pmatrix}, \tag{6}$$

which is formally equivalent to the Jones matrix of a standard waveplate with a complex birefringence parameter. When θ is uniform

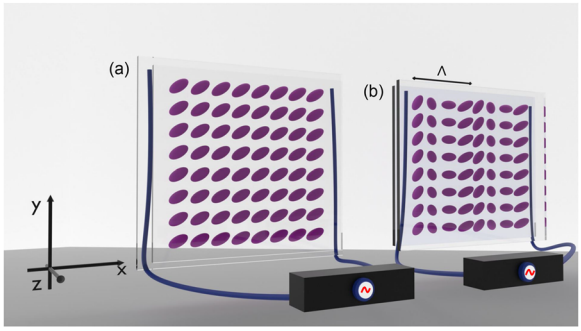

FIG. 1. Dichroic LCMSs. (a) Homogenous LCMS and (b) inhomogeneous LCMS, with the latter exhibiting a periodic pattern along the *x* axis.

across the transverse plane, we refer to these devices as homogeneous LCMSs [see Fig. 1(a)]. However, LC molecules can be photoaligned according to a specific pattern $\theta(x, y)$, as shown in Fig. 1(b). Further details on the fabrication of the samples are provided in Sec. IV. In the following, we provide a characterization of dichroic LCMSs in both configurations.

A. Dichroic homogeneous LCMSs

The dichroic coefficient η is wavelength-dependent. To characterize this spectral response, absorption measurements are carried out for homogeneous samples. From the results reported in Fig. 2, it is clear that the dichroic power of the LCMSs significantly decreases above 630 nm, where the absorption of extraordinary and ordinary components is comparable. Accordingly, $\lambda = 532$ nm is selected as the operating wavelength to maximize the dichroism of our devices while aligning with the availability of laser sources in our laboratory. The nematic mixture E7 (from Merck) is used as the LC host, having refractive indices $n_o = 1.5277$ and $n_e = 1.7538$ at the operating wavelength.[48] The application of an external electric field along z causes the LC molecules to tilt out of plane toward the z-axis (see Fig. 1), altering the extraordinary refractive index of the LC layer. As the field strength increases, this index approaches the value of the ordinary refractive index. In conventional LCMSs, this effect is used to tune the effective birefringence parameter δ.[29,49] Being the orientation of dye molecules coupled to that of LCs, in the case of dichroic LCMSs, the dichroic power of the cell changes as well when adjusting

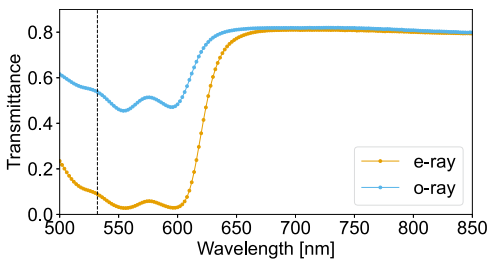

FIG. 2. Spectral characterization of dichroic LCMSs. Measured transmittance of extraordinary and ordinary components for different wavelengths. A vertical bar at $\lambda = 532$ nm indicates the conditions of our experiment.

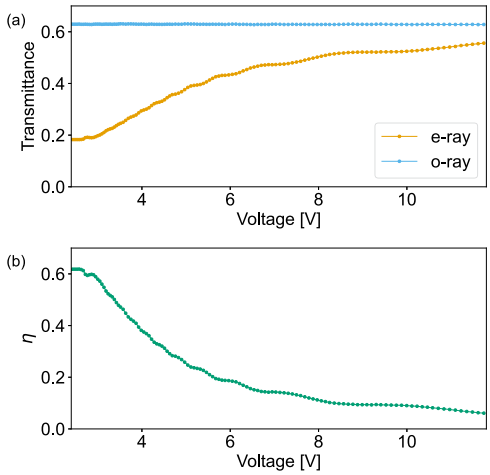

FIG. 3. Linear dichroism as a function of voltage. (a) Measured transmittance of extraordinary and ordinary components at $\lambda = 532$ nm for different input voltages. (b) Extracted dichroic parameter η from the recorded transmittance. At high voltages, the dichroic power of the cells vanishes.

the external electric field. We characterized this effect by recording the transmitted power for the extraordinary and ordinary waves at different values of the applied voltage. In particular, an oscillating square wave signal at ~4 KHz is used. From the transmittance curves shown in Fig. 3(a), the dichroic parameter η is extracted at each voltage [cf. Eqs. (3) and (4)],

$$\eta = \frac{1}{2} \log \frac{P_o}{P_e}, \tag{7}$$

where P_o (P_e) is the transmitted power of the ordinary (extraordinary) component. Even if a closed-form relation for $\eta(V)$ is not reported, the observed voltage-dependent trend can be explained as follows: as the applied voltage increases, the absorption along the ordinary axis remains unchanged, while the field-induced tilt of the LCs toward the propagation direction reduces the absorption along the extraordinary axis. At low voltages, the LCs are nearly orthogonal to the propagation axis, leading to a maximum difference between the absorption coefficients, which results in the maximum value of η [see Fig. 3(b)]. In the limiting case where the LCs are fully aligned with the electric field, the components along the ordinary and extraordinary axes become indistinguishable, leading to minimum dichroism. In all figures showing the response of these devices to the applied electric field, the reported voltage values represent peak-to-peak amplitudes.

Homogeneous LCMSs are also characterized with circularly polarized light. In particular, we illuminate the sample with a left-handed input beam and project the transmitted light on the two orthogonal circular polarization components. From Eq. (6), we obtain

$$\begin{aligned} P_{LR} &= e^{-\bar{\eta}} \left| \sin \frac{\zeta}{2} \right|^2 = e^{-\bar{\eta}} \frac{\cosh \eta - \cos \delta}{2}, \\ P_{LL} &= e^{-\bar{\eta}} \left| \cos \frac{\zeta}{2} \right|^2 = e^{-\bar{\eta}} \frac{\cosh \eta + \cos \delta}{2}, \end{aligned} \tag{8}$$

where P_{LR} (P_{LL}) is the power of the right (left) projection, corresponding to the converted (unconverted) fraction of incoming light. In the limit $\eta \to 0$, up to the attenuation factor $e^{-\eta}$, the functionality of standard LCMSs is recovered, with the unitary condition expressed as

$$P_{LR,\eta\to 0} + P_{LL,\eta\to 0} = \sin^2\frac{\delta}{2} + \cos^2\frac{\delta}{2} = 1. \tag{9}$$

The joint presence of birefringence and dichroism, and their dependence on the external field, can be revealed by measuring the transmitted power of the converted and unconverted light at different voltages. In particular, the relative amplitude of the minima and maxima of the two components does not stay constant [see Fig. 4(a)], as both the birefringence δ and the dichroic parameter η depend on the applied voltage, unlike non-dichroic LCMSs [see Fig. 4(b)]. Furthermore, the minima of both P_{LR} and P_{LL}, which are expected to vanish in the unitary case, take finite values due to the presence of dichroism. Nevertheless, as in the case of standard LCMSs, the maxima (minima) of the converted (unconverted) component correspond approximately to an effective birefringence equal to half-wave retardation [see Eq. (8)]: $\delta = (2n+1)\pi$, with n being an integer number. Vice versa, the minima (maxima) of the converted (unconverted) component correspond to full-wave retardation: $\delta = 2n\pi$. Quarter-wave retardation ($\delta = (2n+1)\pi/2$) is obtained when $P_{LR} = P_{LL}$.

B. Dichroic patterned LCMSs

As discussed above, LC molecules can be photoaligned so as to match a specific pattern. Here, we focus on linear polarization gratings,[40] where the optic-axis orientation features a 1D linear modulation, $\theta(x) = \pi x/\Lambda$. Λ is a characteristic distance, set to 5 mm in our experiment, representing the spatial period of the grating. Originally introduced in the context of polarization holography,[40] they have recently been used for the simulation of 2D quantum walks in the light transverse-momentum space,[38] where they have been dubbed g-plates.[38] Such devices have also been recently employed for enhanced metrological protocols.[37]

Polarization gratings, or g-plates, act by deflecting incident light in opposite directions depending on the input polarization.[40,50,51] Figure 5(a) shows the pattern emerging when observing a dichroic g-plate between crossed polarizers. This is very similar to the typical fringe pattern of a non-dichroic cell, having bright and dark fringes alternating with a period $\Lambda/2$, as illustrated in Fig. 5(b). However, the dichroic character of the plate can be revealed by removing the analyzer (A) while maintaining the polarizer (P). In fact, the differential absorption of light by dye molecules reveals the grating structure even without an analyzer [see Figs. 5(c) and 5(d)]. In this case, the spatial period of the fringes is Λ.

The g-plate device modifies the input beam by adding a quantized amount of transverse momentum $\pm\Delta k_\perp$, given by $\Delta k_\perp = 2\pi/\Lambda$, depending on the input polarization [cf. Eq. (6)]. In other words, it creates optical modes characterized by a wavefront slightly tilted in the xz plane. These modes carrying discrete units of transverse momentum can be sorted on a CCD camera placed in the focal plane of a converging lens, as long as $w_0 \geq \Lambda$, with w_0 being the input beam waist. In this scenario, the modes appear as separate Gaussian spots arranged on a line.[38] Representative far-field distributions recorded on the camera are shown in the top insets of Fig. 6.

In the following, we provide a characterization of the diffraction efficiency of a dichroic g-plate for linear and circularly polarized input states and for different values of the birefringence parameter, selected as illustrated in Sec. II A. When considering a horizontally polarized input beam, $|H\rangle = (|L\rangle + |R\rangle)/\sqrt{2}$, an ideal non-dichroic g-plate at half-wave retardation can be used to perfectly sort optical modes being left or right polarized, by adding a single unit of transverse momentum $\Delta k_\perp$ with opposite signs. This is not the case for a dichroic plate, where the dichroism is responsible for a residual fraction of incoming light sent to the zero order, as shown in Fig. 6(a). A similar behavior is observed for a left-circular input, wherein only the first diffraction order is expected in the non-dichroic case [see Fig. 6(b)]. In the case of quarter-wave plate retardation, the dichroic character manifests itself as a global attenuation equally

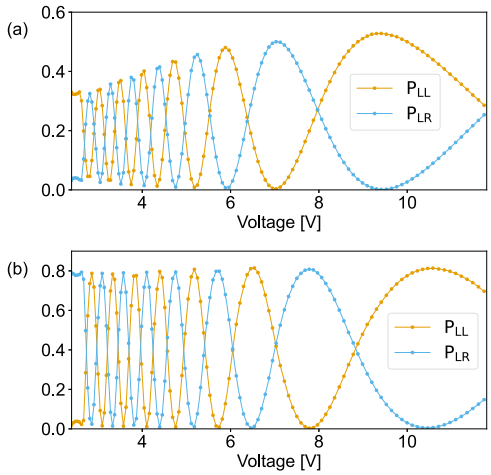

FIG. 4. Characterization of dichroic LCMSs with circularly polarized light. Measured power (normalized to the total input power) of the converted (P_{LR}) and unconverted (P_{LL}) circular polarization components from (a) a dichroic and (b) a non-dichroic LCMS. The varying ratio between the maxima and minima is a signature of the dichroic character of the cell.

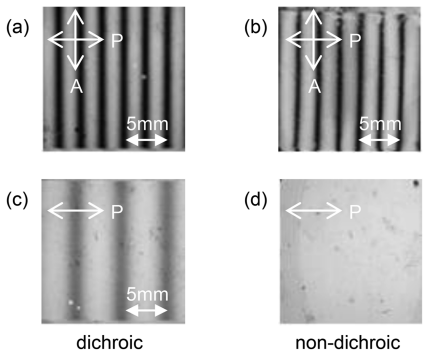

FIG. 5. LC polarization gratings. (a) A dichroic and (b) a non-dichroic LCMS, patterned with a grating structure, are observed between crossed polarizers P and A. When removing the analyzer A, (c) the grating pattern is clearly visible in the dichroic device, while (d) it is invisible in standard LCMSs.

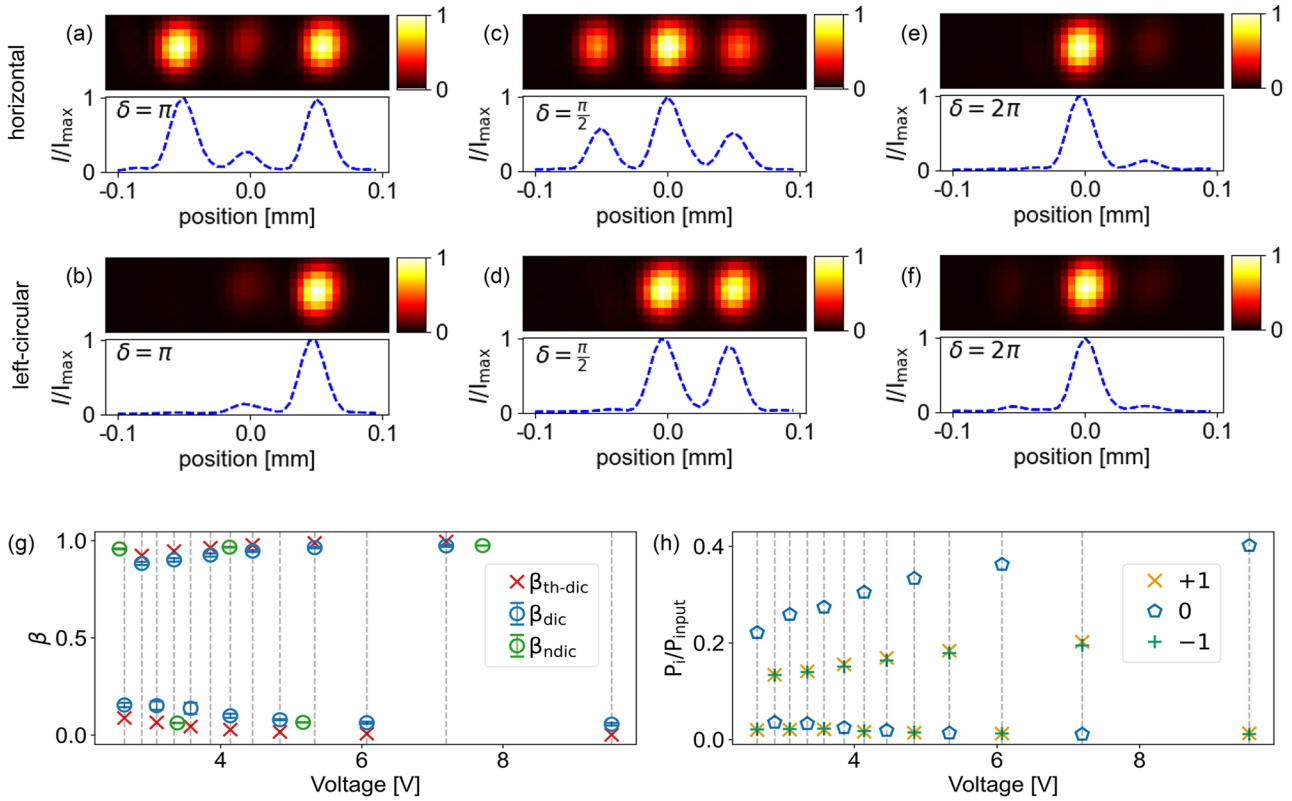

FIG. 6. Diffraction from a dichroic *g*-plate. Measured far-field distributions and corresponding line intensity profiles from a dichroic *g*-plate operating at half-wave (a, b), quarter-wave (c, d), and full-wave (e, f) retardation, for horizontally (top) and left-circularly (bottom) polarized input states. Retardations corresponding to $\delta = \pi$, $\frac{\pi}{2}$, and 2π are obtained by applying a peak-to-peak voltage equal to 2.82, 2.95, and 3.05 V, respectively. (g) Measured values of the diffraction efficiency β of a dichroic *g*-plate (blue circles) at voltages corresponding to full-wave and half-wave retardation, obtained when shining the cell with horizontally polarized light, compared with a non-dichroic cell (green circles) and with theoretical predictions based on Eq. (8) (red crosses). As predicted from Eq. (8), the maxima and minima of the diffraction efficiency do not stay constant, as at larger values of the applied voltage, the dichroic power of the cell is reduced. (h) Transmittance of individual diffraction orders generated by using a dichroic *g*-plate, obtained by dividing the power of each mode by the total input power.

affecting the diffracted and unmodulated light, as shown in Figs. 6(c) and 6(d). An interesting case is provided by full-wave retardation, where non-dichroic *g*-plates act as the identity operator, while the presence of dichroism in our samples drives a small portion of the input light to the first diffraction orders [see Figs. 6(e) and 6(f)].

By collecting intensity distributions in the far field, as those illustrated in Fig. 6, the diffraction efficiency β of the dichroic *g*-plate at several values of the applied voltage is extracted. In particular, we compute as P_{-1}, P_0, P_1 the integrated intensity of the corresponding diffraction orders. β is then obtained as

$$\beta = \frac{P_{-1} + P_1}{P_{-1} + P_1 + P_0}. \tag{10}$$

Essentially, it measures the ratio between the correctly diffracted light and the total transmitted light, assuming that there is no diffraction into higher-order modes, which is the case for linear phase gradients. Horizontal polarization is used as the input, and the voltages corresponding to half-wave and full-wave retardation are considered for this analysis. As expected, the maxima (minima) of β correspond to half-wave (full-wave) retardation. However, unlike non-dichroic devices, the diffraction efficiency does not take the same values at different maxima and minima, as increasing the voltage reduces the dichroic power of the cell (cf. Figure 3). Experimental results are reported in Fig. 6(g). They are compared with theoretical estimates, extracted from Eq. (8) with values of η reported in Fig. 3(b), and with the diffraction efficiency measured from a non-dichroic sample. In the latter case, measurements were taken for a *g*-plate with a smaller thickness, $d = 6\ \mu$m, resulting in a reduced number of voltage levels at which the device operates at half-wave and full-wave retardation. Figure 6(h) shows the transmittance of each diffraction order expected for our dichroic grating.

Finally, we assess the time response of our devices by measuring the switching time of a dichroic *g*-plate, defined as the time required to switch from full-wave to half-wave retardation and vice versa, after the voltage has changed. This time is estimated by monitoring the complete switching of the transmitted power of the light converted component from a minimum to a maximum value and vice versa. In this realization, we consider all available transitions at successive voltage levels, as reported in Fig. 7. The sampling time

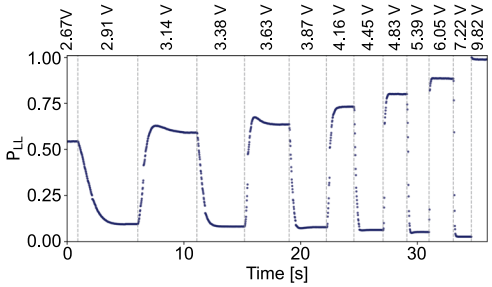

FIG. 7. Switching time. We measure the switching time of a dichroic *g*-plate at successive voltages corresponding to full-wave and half-wave retardations. The vertical lines indicate when the voltage switches to the values reported at the top. The response time is on the order of 1 s at low voltages, while it becomes faster in the high-voltage regime. The smallest sampling time of the power meter was used, corresponding to ~20 ms.

from the power meter is about 20 ms. As expected, the response time of the cell is slower at low voltages ($\simeq$ 1 s), while it becomes faster at higher voltages ($\simeq$ 100 ms). This is due to the larger torque induced by stronger fields. In the future, the slow response at low voltages could be overcome by using thinner cells[49] or introducing a pre-tilt angle at the alignment surface.

III. CONCLUSION

We introduced a new class of LCMSs that exhibit polarization-dependent losses. The optical behavior of these devices can be described by a non-unitary Jones matrix, formally equivalent to that of a standard waveplate with a complex birefringence parameter. This model has been experimentally validated on both homogeneous and structured metasurfaces, where the spin–orbit functionality embeds the dichroic feature.

We demonstrated that the application of an external voltage serves as a convenient control for tuning the dichroic character of the cell, with the only limitation being that the birefringence and dichroic properties are inherently coupled and cannot be adjusted independently. The new devices hold great promise for the simulation of non-unitary dynamics and non-Hermitian topological phases.[52–56]

Our investigation was carried out assuming a negligible nonlinear response from the dye, typically associated with photoinduced reorientation of LC molecules.[47] However, we expect small nonlinear effects to still be measurable at our operating power ($\lesssim$ 3 mW),[47] here possibly manifesting as larger deviations from the theoretical description. Incorporating the nonlinear effects into our model will eventually require accounting for both the dye electronic structure and its intermolecular interactions.

IV. METHODS

A. Fabrication

Two glass plates, pre-coated with a thin film of ITO (indium tin oxide, a transparent conductive material), undergo two-stage cleaning in an ultra-sonication chamber, the first with a 5% solution of phosphate-free alkaline detergent and distilled water and the second with distilled water only, both for 60 min at 60°. The plates are then dried in the oven for 60 min at 100°. This is followed by a 45-min ozone–UV exposure, facilitating the subsequent azo-dye deposition. The glass plates are spin-coated with a thin film of photosensitive azo-dye. After spin-coating, the plates are sandwiched together with the help of 17 μm silica spacers. The desired pattern is imprinted using a well-established photoalignment technique,[29] allowing for the azo-dye molecules to be oriented point by point by rotating the linear polarization of an incident beam at 445 nm. After photoalignment, the cell is eventually filled with a mixture of nematic liquid crystals saturated with 1,4-diaminoanthraquinone, which penetrates by capillarity the sample pre-heated at 100°.

ACKNOWLEDGMENTS

We thank Moritsugu Sakamoto for insightful discussion. This work was supported by the PNRR MUR Project No. PE0000023-NQSTI.

AUTHOR DECLARATIONS

Conflict of Interest

The authors declare no conflicts of interest.

Author Contributions

Paola Savarese and Sarvesh Bansal contributed equally to this work.

Paola Savarese: Data curation (equal); Formal analysis (equal); Investigation (equal); Methodology (equal); Software (equal); Validation (equal); Visualization (equal). **Sarvesh Bansal**: Data curation (equal); Formal analysis (equal); Investigation (equal); Methodology (equal); Software (equal); Validation (equal); Visualization (equal). **Maria Gorizia Ammendola**: Data curation (equal); Investigation (equal); Validation (equal). **Raouf Barboza**: Data curation (equal); Formal analysis (equal); Investigation (equal); Validation (equal); Writing – review & editing (equal). **Marcella Salvatore**: Data curation (equal); Investigation (equal); Methodology (equal). **Stefano Luigi Oscurato**: Data curation (equal); Investigation (equal); Methodology (equal). **Bruno Piccirillo**: Data curation (equal); Formal analysis (equal); Investigation (equal); Validation (equal); Writing – review & editing (equal). **Francesco Di Colandrea**: Conceptualization (equal); Formal analysis (equal); Investigation (equal); Methodology (equal); Supervision (equal); Writing – original draft (equal); Writing – review & editing (equal). **Lorenzo Marrucci**: Data curation (equal); Formal analysis (equal); Investigation (equal); Supervision (equal); Validation (equal); Writing – review & editing (equal). **Filippo Cardano**: Conceptualization (equal); Formal analysis (equal); Investigation (equal); Methodology (equal); Supervision (equal); Writing – original draft (equal); Writing – review & editing (equal).

DATA AVAILABILITY

The data that support the findings of this study are available from the corresponding author upon reasonable request.

REFERENCES

[1] K. Y. Bliokh, F. J. Rodríguez-Fortuño, F. Nori, and A. V. Zayats, "Spin–orbit interactions of light," Nat. Photonics **9**, 796 (2015).

[2] F. Cardano and L. Marrucci, "Spin–orbit photonics," Nat. Photonics **9**, 776 (2015).

[3] D. Hakobyan and E. Brasselet, "Left-handed optical radiation torque," Nat. Photonics **8**, 610 (2014).

[4] E. Alonso Guzmán and A. V. Arzola, "Enhancing near-field optical tweezers by spin-to-orbital angular momentum conversion," J. Opt. Soc. Am. B **39**, 1233 (2022).

[5] J. Petersen, J. Volz, and A. Rauschenbeutel, "Chiral nanophotonic waveguide interface based on spin-orbit interaction of light," Science **346**, 67 (2014).

[6] S. Slussarenko, A. Alberucci, C. P. Jisha, B. Piccirillo, E. Santamato, G. Assanto, and L. Marrucci, "Guiding light via geometric phases," Nat. Photonics **10**, 571 (2016).

[7] O. G. Rodríguez-Herrera, D. Lara, K. Y. Bliokh, E. A. Ostrovskaya, and C. Dainty, "Optical nanoprobing via spin-orbit interaction of light," Phys. Rev. Lett. **104**, 253601 (2010).

[8] R. Dorn, S. Quabis, and G. Leuchs, "Sharper focus for a radially polarized light beam," Phys. Rev. Lett. **91**, 233901 (2003).

[9] K. Y. Bliokh, E. A. Ostrovskaya, M. A. Alonso, O. G. Rodríguez-Herrera, D. Lara, and C. Dainty, "Spin-to-orbital angular momentum conversion in focusing, scattering, and imaging systems," Opt. Express **19**, 26132 (2011).

[10] F. Cardano, F. Massa, H. Qassim, E. Karimi, S. Slussarenko, D. Paparo, C. de Lisio, F. Sciarrino, E. Santamato, R. W. Boyd, and L. Marrucci, "Quantum walks and wavepacket dynamics on a lattice with twisted photons," Sci. Adv. **1**, e1500087 (2015).

[11] T. Ozawa, H. M. Price, A. Amo, N. Goldman, M. Hafezi, L. Lu, M. C. Rechtsman, D. Schuster, J. Simon, O. Zilberberg, and I. Carusotto, "Topological photonics," Rev. Mod. Phys. **91**, 015006 (2019).

[12] K. Y. Bliokh, D. Smirnova, and F. Nori, "Quantum spin hall effect of light," Science **348**, 1448 (2015).

[13] J. Wang, L. Shi, and J. Zi, "Spin hall effect of light via momentum-space topological vortices around bound states in the continuum," Phys. Rev. Lett. **129**, 236101 (2022).

[14] M. Kim, D. Lee, Y. Yang, Y. Kim, and J. Rho, "Reaching the highest efficiency of spin hall effect of light in the near-infrared using all-dielectric metasurfaces," Nat. Commun. **13**, 2036 (2022).

[15] M. Sotto, K. Debnath, I. Tomita, and S. Saito, "Spin-orbit coupling of light in photonic crystal waveguides," Phys. Rev. A **99**, 053845 (2019).

[16] M. Huang, Q. Chen, Y. Liu, C. Zhang, R. Zhang, J. Yuan, and D. Zhang, "One-dimensional photonic crystal enhancing spin-to-orbital angular momentum conversion for single-particle tracking," Light Sci. Appl. **13**, 268 (2024).

[17] M. El Ketara and E. Brasselet, "Self-induced nonlinear spin–orbit interaction of light in liquid crystals," Opt. Lett. **37**, 602 (2012).

[18] K. Rechcińska, M. Król, R. Mazur, P. Morawiak, R. Mirek, K. Łempicka, W. Bardyszewski, M. Matuszewski, P. Kula, W. Piecek, P. G. Lagoudakis, B. Piętka, and J. Szczytko, "Engineering spin-orbit synthetic Hamiltonians in liquid-crystal optical cavities," Science **366**, 727 (2019).

[19] M. Muszyński, P. Oliwa, P. Kokhanchik, P. Kapuściński, E. Oton, R. Mazur, P. Morawiak, W. Piecek, P. Kula, W. Bardyszewski, B. Piętka, D. Bobylev, D. Solnyshkov, G. Malpuech, and J. Szczytko, "Electrically tunable spin-orbit coupled photonic lattice in a liquid crystal microcavity," Laser Photonics Rev. **19**, 2400794 (2025).

[20] J. S. Eismann, L. Ackermann, B. Kantor, S. Nechayev, M. Z. Alam, R. Fickler, R. W. Boyd, and P. Banzer, "Enhanced spin–orbit coupling in an epsilon-near-zero material," Optica **9**, 1094 (2022).

[21] E. Karimi, S. A. Schulz, I. De Leon, H. Qassim, J. Upham, and R. W. Boyd, "Generating optical orbital angular momentum at visible wavelengths using a plasmonic metasurface," Light Sci. Appl. **3**, e167 (2014).

[22] P. Genevet, F. Capasso, F. Aieta, M. Khorasaninejad, and R. Devlin, "Recent advances in planar optics: From plasmonic to dielectric metasurfaces," Optica **4**, 139 (2017).

[23] M. Zhang, M. Pu, F. Zhang, Y. Guo, Q. He, X. Ma, Y. Huang, X. Li, H. Yu, and X. Luo, "Plasmonic metasurfaces for switchable photonic spin–orbit interactions based on phase change materials," Adv. Sci. **5**, 1800835 (2018).

[24] R. C. Devlin, M. Khorasaninejad, W. T. Chen, J. Oh, and F. Capasso, "Broadband high-efficiency dielectric metasurfaces for the visible spectrum," Proc. Natl. Acad. Sci. U. S. A. **113**, 10473 (2016).

[25] A. Ambrosio, "Structuring visible light with dielectric metasurfaces," J. Opt. **20**, 113002 (2018).

[26] A. H. Dorrah and F. Capasso, "Tunable structured light with flat optics," Science **376**, eabi6860 (2022).

[27] I. V. Kasyanova, M. V. Gorkunov, V. V. Artemov, A. R. Geivandov, A. V. Mamonova, and S. P. Palto, "Liquid crystal metasurfaces on micropatterned polymer substrates," Opt. Express **26**, 20258 (2018).

[28] H. Larocque, J. Gagnon-Bischoff, F. Bouchard, R. Fickler, J. Upham, R. W. Boyd, and E. Karimi, "Arbitrary optical wavefront shaping via spin-to-orbit coupling," J. Opt. **18**, 124002 (2016).

[29] A. Rubano, F. Cardano, B. Piccirillo, and L. Marrucci, "Q-Plate technology: A progress review [invited]," J. Opt. Soc. Am. B **36**, D70 (2019).

[30] L. Marrucci, C. Manzo, and D. Paparo, "Pancharatnam-berry phase optical elements for wave front shaping in the visible domain: Switchable helical mode generation," Appl. Phys. Lett. **88**, 221102 (2006).

[31] L. Marrucci, C. Manzo, and D. Paparo, "Optical spin-to-orbital angular momentum conversion in inhomogeneous anisotropic media," Phys. Rev. Lett. **96**, 163905 (2006).

[32] L. Marrucci, E. Karimi, S. Slussarenko, B. Piccirillo, E. Santamato, E. Nagali, and F. Sciarrino, "Spin-to-orbital conversion of the angular momentum of light and its classical and quantum applications," J. Opt. **13**, 064001 (2011).

[33] L. Yan, P. Gregg, E. Karimi, A. Rubano, L. Marrucci, R. Boyd, and S. Ramachandran, "Q-plate enabled spectrally diverse orbital-angular-momentum conversion for stimulated emission depletion microscopy," Optica **2**, 900 (2015).

[34] V. D'Ambrosio, E. Nagali, S. P. Walborn, L. Aolita, S. Slussarenko, L. Marrucci, and F. Sciarrino, "Complete experimental toolbox for alignment-free quantum communication," Nat. Commun. **3**, 961 (2012).

[35] A. Sit, F. Bouchard, R. Fickler, J. Gagnon-Bischoff, H. Larocque, K. Heshami, D. Elser, C. Peuntinger, K. Günthner, B. Heim, C. Marquardt, G. Leuchs, R. W. Boyd, and E. Karimi, "High-dimensional intracity quantum cryptography with structured photons," Optica **4**, 1006 (2017).

[36] V. D'Ambrosio, N. Spagnolo, L. Del Re, S. Slussarenko, Y. Li, L. C. Kwek, L. Marrucci, S. P. Walborn, L. Aolita, and F. Sciarrino, "Photonic polarization gears for ultra-sensitive angular measurements," Nat. Commun. **4**, 2432 (2013).

[37] R. Barboza, A. Babazadeh, L. Marrucci, F. Cardano, C. de Lisio, and V. D'Ambrosio, "Ultra-sensitive measurement of transverse displacements with linear photonic gears," Nat. Commun. **13**, 1080 (2022).

[38] A. D'Errico, F. Cardano, M. Maffei, A. Dauphin, R. Barboza, C. Esposito, B. Piccirillo, M. Lewenstein, P. Massignan, and L. Marrucci, "Two-dimensional topological quantum walks in the momentum space of structured light," Optica **7**, 108 (2020).

[39] F. Di Colandrea, A. Babazadeh, A. Dauphin, P. Massignan, L. Marrucci, and F. Cardano, "Ultra-long quantum walks via spin–orbit photonics," Optica **10**, 324 (2023).

[40] T. Todorov, L. Nikolova, and N. Tomova, "Polarization holography 2: Polarization holographic gratings in photoanisotropic materials with and without intrinsic birefringence," Appl. Opt. **23**, 4588 (1984).

[41] T. Zhan, J. Xiong, G. Tan, and S.-T. Wu, "Absorption-based polarization gratings," Opt. Express **28**, 13907 (2020).

[42] N. A. Rubin, P. Chevalier, M. Juhl, M. Tamagnone, R. Chipman, and F. Capasso, "Imaging polarimetry through metasurface polarization gratings," Opt. Express **30**, 9389 (2022).

[43] R. Caputo, I. Trebisacce, L. De Sio, and C. Umeton, "Jones matrix analysis of dichroic phase retarders realized in soft matter composite materials," Opt. Express **18**, 5776 (2010).

[44] M. Suzuki, S. Ohara, M. Sakamoto, K. Noda, T. Sasaki, N. Kawatsuki, and H. Ono, "Temperature dependence of the diffraction efficiency of circular polarization gratings made by liquid crystal molecules with anisotropic absorption," Opt. Mater. Express **14**, 1857 (2024).

[45] P. Yeh and C. Gu, *Optics of Liquid Crystal Displays, Vol. 67* (John Wiley & Sons, 2009).
[46] S. M. Kelly, *Flat Panel Displays: Advanced Organic Materials* (The Royal Society of Chemistry, 2000).
[47] L. Marrucci, D. Paparo, M. R. Vetrano, M. Colicchio, E. Santamato, and G. Viscardi, "Role of dye structure in photoinduced reorientation of dye-doped liquid crystals," J. Chem. Phys. **113**, 10361 (2000).
[48] See Shelf/Other-miscellaneous materials, Book/E7, Pages/Tkachenko *et al.*, 2006, at https://refractiveindex.info/?shelf=other&book=E7&page=Tkachenko-e for reference values of the refractive indices of E7.
[49] B. Piccirillo, V. D'Ambrosio, S. Slussarenko, L. Marrucci, and E. Santamato, "Photon spin-to-orbital angular momentum conversion via an electrically tunable q-plate," Appl. Phys. Lett. **97**, 241104 (2010).
[50] F. Gou, F. Peng, Q. Ru, Y.-H. Lee, H. Chen, Z. He, T. Zhan, K. L. Vodopyanov, and S.-T. Wu, "Mid-wave infrared beam steering based on high-efficiency liquid crystal diffractive waveplates," Opt. Express **25**, 22404 (2017).
[51] M. Sakamoto, H. T. Nhan, K. Noda, T. Sasaki, T. Kamei, T. Sakai, Y. Hattori, N. Kawatsuki, and H. Ono, "Polarized beam steering using multiply-cascaded rotating polarization gratings," Appl. Opt. **60**, 2062 (2021).
[52] X. Zhan, L. Xiao, Z. Bian, K. Wang, X. Qiu, B. C. Sanders, W. Yi, and P. Xue, "Detecting topological invariants in nonunitary discrete-time quantum walks," Phys. Rev. Lett. **119**, 130501 (2017).
[53] Z. Gong, Y. Ashida, K. Kawabata, K. Takasan, S. Higashikawa, and M. Ueda, "Topological phases of non-hermitian systems," Phys. Rev. X **8**, 031079 (2018).
[54] E. J. Bergholtz, J. C. Budich, and F. K. Kunst, "Exceptional topology of non-Hermitian systems," Rev. Mod. Phys. **93**, 015005 (2021).
[55] H. Nasari, G. G. Pyrialakos, D. N. Christodoulides, and M. Khajavikhan, "Non-Hermitian topological photonics," Opt. Mater. Express **13**, 870 (2023).
[56] P. Savarese, S. Bansal, M. G. Ammendola, L. Amato, R. Barboza, B. Piccirillo, F. Di Colandrea, L. Marrucci, and F. Cardano, Programmable non-Hermitian photonic quantum walks via dichroic metasurfaces, arXiv:2503.05072 (2025).